Dust Aerosol Retrieval Over the Oceans with the MODIS/VIIRS Dark Target algorithm. Part I: Dust Detection

Yaping Zhou[1,2], Robert C. Levy [2], Lorraine A. Remer[1],
Shana Mattoo[2,3], Yingxi Shi[1,2], Chenxi Wang[1,2]
[1]University of Maryland Baltimore County, [2] NASA Goddard Flight Center, [3]Science Systems and Applications, Inc. Center,

Abstract

To prepare for implementation of a new aerosol retrieval specifically designed for dust aerosol over ocean in the operational Dark Target (DT) algorithms for the Moderate-resolution Imaging Spectrometer (MODIS) and Visible Infrared Imaging Radiometer Suite (VIIRS) satellite sensors, we focus on the challenge of detecting dust. We first survey the literature on existing dust detection algorithms and then develop an innovative algorithm that combines near-UV (deep blue), visible, and thermal infrared (TIR) wavelength spectral tests. The new detection algorithm is applied to Terra and Aqua MODIS granules and compared with other dust detection possibilities from existing MODIS products. Quantitative evaluation of the new dust detection algorithm is conducted using both a collocated AERONET - MODIS dataset and collocated CALIPSO – MODIS dataset. From comparison with both AERONET and CALIOP measurements, we estimate the new dust detection algorithm detects about 30% of weakly dusty pixels and more than 80% of heavily dusty pixels, with false detections in the range of 1-2%. The very low false detection rate is particularly noteworthy in comparison with existing literature. Compared with the dust flag currently available as part of the MODIS cloud mask product (MOD35/MYD35), and dust classification based on commonly used thresholds with AOD and AE, the new dust detection algorithm finds more dusty pixels and fewer false detections.

1. Introduction

Mineral dust aerosols arise from windblown soils, and have a multitude of impacts on weather and climate, air quality, public health, and ecosystems. Dust aerosol affects global and regional climate through direct radiative forcing and indirect interaction with cloud and precipitation processes (Miller & Tegen, 1998; Harrison et al., 2001; Kaufman et al., 2002; Yu et al., 2006; Shell & Somerville 2007; Rosenfeld et al., 2011; Zhao et al., 2011; Kok et al., 2018). Dust aerosols can significantly impact air quality and the human respiratory system (Griffin 2007; Goudie 2013). Heavy dust storms can impair local transportation and cause damage to infrastructure and crops (Prospero et al., 2003; Goudie & Middleton, 2006; Weinzierl et al., 2012). Mineral dust originating from one region can be transported thousands of kilometers downwind, impacting air quality and ecosystems far beyond its source region (Kaufman et al., 2005; Hsu et a. 2006; Gassó et al., 2010; Yu et al., 2013; 2015; Gaiero et al., 2013; Prospero et al., 2014; Kim et al., 2014). Characterizing global dust distribution is thus very important for climate studies as well as air quality monitoring. Dust aerosol is particularly complex as these particles have a wide range of sizes, shapes and mineralogical compositions, depending on the source region and meteorological conditions. Dust entrained into the atmosphere from a source region is subject to many changes during its thousands of kilometers transit as mixing, humidification and deposition of large particles takes place.

As dust is so complex, satellite remote sensing provides the global observations for characterizing global dust distribution. Remote sensing of dust or other aerosol particles is commonly performed by using the spectral signatures in observed radiances that arise from the interactions between the light and the atmospheric particulates. The size, shape and chemical compositions of particles determine their absorption and scattering properties and the radiances received by a remote sensing instrument. These measurements, when converted into either reflectance in the UV, visible, Near IR channels or brightness temperature in the infrared, are used to infer the columnar integrated mass and optical properties of the particles. However in addition to the dust we are trying to observe, factors such as surface reflectivity, clouds, and other types of

aerosols and molecular scattering contribute to the spectral signatures received by the sensors. Thus, identifying dust and retrieving its optical properties is a great challenge.

The Moderate-resolution Imaging Spectrometer (MODIS) instruments on board the Terra and Aqua satellites have been observing the earth's cloud, aerosol and surface since their launches in 2000 and 2002, respectively. MODIS comprises 36 spectral channels from 0.41 μm to 15 μm with a nominal (nadir) resolution of 250, 500, or 1000 m at nadir depending on band, and has a swath width of approximately 2300 km. For aerosol retrievals, currently there are three operational retrieval algorithms, namely, Dark-Target (DT; Levy et al., 2013), Deep Blue (DB; Hsu et al., 2019) and Multi-angle Implementation of Atmospheric Correction (MAIAC; Lyapustin et al., 2018), all developed at NASA's Goddard Space Flight Center.

The DT aerosol retrieval algorithm consists of two independent components, one for ocean (DT-O; Tanré et al.,1997; Remer et al., 2005; Levy et al., 2013), and one for the dark land surfaces such as vegetation (DT-L; Levy et al., 2007a,b; Levy et al., 2010, Levy et al., 2013). The DT algorithm relies on observing the contrast (and spectral dependence) of aerosol reflectance over dark surfaces and oceans. The algorithm (both land and ocean) follows a lookup table (LUT) approach, i.e., the Top-of-atmosphere (TOA) spectral reflectance is pre-calculated using scattering and radiative transfer (RT) codes (Wiscombe, 1980; Dubovik et al., 2002; Evans & Stephens, 1991; Ahmad & Fraser, 1982) for predefined aerosol, surface and atmospheric properties. The ocean LUTs contain four fine aerosol models and five coarse models, in an effort to represent all aerosol types. The DT-O retrieval algorithm selects one fine mode and one coarse mode aerosol with an adjustable fraction that minimizes the difference between the LUT reflectance and observed TOA reflectance in six wavelengths (0.55, 0.65, 0.86, 1.2, 1.6 and 2.13 μm). The retrieved quantities include total aerosol optical depth (AOD at 0.55 μm), Angstrom Exponent (AE1) derived from the AOD at 0.55 μm and 0.86 μm and a Fine Mode Fraction (FMF) that estimates the relative mixing between the fine mode and coarse mode aerosols.

Dust aerosols are predominantly non-spherical in shape (Chou et al., 2008). The DT-land has incorporated a non-spherical dust model (Levy et al., 2007a). However, the current MODIS DT-O algorithm still does not have a non-spherical dust model, which creates bias in the retrieved AOD, FMF and AE (shown in Section 5.2). While it may be tempting to simply replace the DT-O algorithm's current spherical coarse models with new models corresponding to non-spherical particles (without changing the rest of the algorithm), it does not work. Choosing the right dust model is not trivial as dust particles can take on different sizes, shapes and chemical compositions and an ill-represented dust model may make the retrieval worse. Additionally, there is no guarantee that the algorithm would reliably choose non-spherical models for dust and spherical models for non-dust aerosol, possibly further degrading the results of the retrieval.

Therefore our strategy is to use two steps, first identify likely dust pixels, and then retrieve the AOD, AE and FMF using an appropriate dust model. In this Part I paper, we focus on dust detection, and organize as follows. Section 2 describes the data used in this work. Section 3 reviews dust detection in the current literature and summarizes our new dust identification algorithm. Section 4 evaluates the new dust detection algorithm with sample granules, by collocating and comparing to ground-based sun photometer and satellite-based lidar data. Section 5 shows the global dust distribution in two dust heavy months. A brief summary and discussion is provided in Section 6.

2. Data

The primary data used in the study are MODIS Level 1B calibrated TOA reflectance products (MxD02) (http://mcst.gsfc.nasa.gov/content/l1b-documents) and Collection C6 Level 2 aerosol products MxD04 (Levy et al., 2013) (where x is substituted by O for Terra and Y for Aqua). The MxD02 contains reflectance and radiance data at three native resolutions (i.e., 0.25 km, 0.5 km or 1.0 km at nadir, depending on band). whereas the dark-target algorithm aggregates these observations into 3x3 or 10x10 boxes as retrieval units. The MxD04_L2 products used here include Aerosol Optical Depth (AOD), Angstrom Exponent (AE), and Fine Mode Fraction (FMF) reported at 10x10 km

(nadir) resolution. In addition to the retrieved aerosol properties, a MxD04 data point contains the clear-sky reflectance values used in the retrieval, quality assurance (confidence) estimates, as well as other ancillary information such as 2-meter surface wind speed from National Centers for Environmental Prediction (NCEP) re-analysis. We also use many of the individual cloud tests and especially the dust flag from the standard MODIS cloud mask product MxD35 (reported at 1 km resolution).

Aerosol measurements from the ground-based Aerosol Robotic Network (AERONET) sun photometers are commonly used for validating satellite aerosol retrievals. AERONET is a global network of Cimel Electronique CE-318 sun-sky radiometers with between 4 and 9 spectral channels. AOD is obtained from direct sun measurements most often at 0.34, 0.38, 0.44, 0.50, 0.67, 0.87, and 1.02 μm with frequency of every 15 min; The high accuracy of AERONET AOD (estimated errors of ~0.01–0.02) makes it widely popular (Eck et al., 1999; Holben et al., 1998). In addition to direct sun measurements, the instruments measure the sky radiance in four spectral bands (0.44, 0.67, 0.87 and 1.02 μm) along the solar principal plane up to nine times a day and along the solar almucantar up to eight times a day. Measurements from almucantar scans are used to retrieve aerosol particle size distribution, spectral complex refractive index and single scattering albedo (SSA) (Dubovik & King, 2000; Dubovik et al., 2001). The majority of traditional AERONET stations are situated inland, with some located near the coast, and very few at small islands in the middle of the ocean. In this work, we use the latest Version 3 products, which provides improved cloud screening and better identification of heavy aerosol events (Giles et al., 2019).

To match the MODIS retrievals with the AERONET measurements, AERONET measurements within ±30 min of the MODIS overpass time are averaged and compared against the values for all the MODIS retrieved pixels located within 0.3° of AERONET stations (Shi et al., 2019). In this way there are many collocations reported at each AERONET or MAN location at every overpass opportunity, since the AERONET or MAN observations are averaged to a single value but the many MODIS retrieved pixels within the match-up circle are not. The MODIS (both Aqua and Terra) - AERONET

collocation data from 2011 will be used for evaluation of the new dust detection algorithm. AERONET AOD measurements at 0.44 μm and 0.67 μm are linearly interpolated in log-log space (i.e. fit by Angstrom exponent) to be compared with MODIS AOD at 0.55 μm. We use the AERONET AOD and AE measurements to identify likely dust situations and compare with the result of the new dust detection algorithm applied to MODIS pixels in near proximity to the AERONET station.

Aerosol measurements from space-borne active sensors such the Cloud-Aerosol Lidar with Orthogonal Polarization (CALIOP) onboard the Cloud-Aerosol Lidar and Infrared Pathfinder Satellite Observation (CALIPSO) (Winker et al., 2013) are frequently used to evaluate the performance of dust detection algorithm designed for passive sensors (Stubenrauch et al., 2013; Ciren & Kondragunta, 2014). CALIPSO was a key member of the Afternoon Constellation of satellites (A-Train) from 2006 to 2018, measuring backscattering profiles at a 30-meter vertical and 333 m along-track resolution at wavelengths of 532 nm and 1064 nm (Winker et al., 2013). CALIOP also measures the perpendicular and parallel signals at 532 nm, along with the depolarization ratio at 532 nm that is frequently used in aerosol/cloud phase discrimination algorithms because of its strong particle shape dependence. The CALIOP Version 4 Level 2 5-km Cloud/Aerosol Layer products not only provide cloud aerosol type information, but a qualitative assignment of aerosol type in each vertical layer, i.e., 'dust', 'smoke', 'polluted dust' or 'marine dust'. A MODIS-Aqua / CALIOP collocated dataset is generated with a strict algorithm that fully considers the spatial differences between the two instruments and parallax effects, as described in Holz et al. (2008). We consider various numbers of CALIOP-identified pure dust aerosol layers in the vertical column to identify dusty pixels that should be detected by the new algorithm applied to MODIS measurements. Note that when we say that a pixel or a scene is 'dusty', we mean that it has been identified as likely containing dust aerosol somewhere within the horizontal or vertical domain.

3.0 Developing a dust detection algorithm for MODIS

3.1 Current dust detection techniques

Many dust detection algorithms have been developed utilizing specific optical properties of dust in the ultraviolet (UV) (Herman et al., 1997), visible (Miller, 2003; Jankowiak & Tanré, 1992; Martins et al., 2002; Kaufman et al., 1997) and infrared (IR) (Evan et al., 2006; Xie, 2009; Zhao et al., 2010; Cho et al., 2013) spectral regions. The absorption Aerosol Index (AAI) derived from Total Ozone Mapping Spectrometer (TOMS) and Ozone Monitoring Instruments (OMI) instruments is a UV-based technique that utilizes the strong absorption of dust and smoke and low-surface reflectivity in UV spectral regions (Herman et al., 1997; Torres et al., 1998, 2007). The AAI relies on the relatively small spectral variations in two UV channels (0.354 μm and 0.388 μm) in the presence of absorbing aerosols as compared to rapid change of Rayleigh scattering in these channels. A Dust Aerosol Index (DAI) computed from slightly longer wavelength in deep blue and blue channels (0.412 μm and 0.490 μm) is employed by the DB aerosol retrieval algorithm for SeaWiFS and MODIS instruments to screen cloud scenes over bright surface (Hsu et al., 2004). Setting a higher threshold for DAI prevents misidentification of dust scenes and cloud. A recent NOAA dust detection algorithm utilizes DAI as a first step to separate absorbing aerosols (dust and smoke) from non-absorbing aerosols (Ciren & Kondragunta, 2014). NOAA's DAI is computed from two close channels in 0.412 μm and 0.440 μm to minimize reflectance changes in surface. Neither AAI or DAI can separate dust from other absorbing aerosols such as smoke. Hence NOAA's dust detection algorithm further uses a NonDust Absorbing Aerosol Index (NDAI), computed from the spectral ratio of 0.412 μm and 2.13 μm channels to separate dust from smoke. The NDAI capitalizes on the fact that dust particles have higher reflectivity in the 2.13 μm band than smoke particles as a result of their larger size. However, the differences in surface reflectance between the two wavelengths are not taken into consideration.

In the visible and NIR wavelengths, since dust is visually brighter than most dark surfaces, i.e., ocean and vegetation, but darker than cloud and sometimes desert, reflectance in visible channels (0.47μm, 0.65μm and 0.87μm) make good first order tests for dust scenes in locations where dust is expected (Tanré & Legrand 1991; Kaufman et al., 2000; Jankowiak & Tanré, 1992; Miller 2003). More sophisticated techniques use the

different spectral variations of dust absorption and scattering in contrast to surface and cloud, and reflectance ratios between blue, red and green channels (i.e., 0.47μm / 0.65μm, 0.65μm / 0.55μm, and 0.55μm / 0.47μm) or normalized reflectance difference such as NDVI have been used for dust detection (Jankowiak & Tanré,1992; Miller 2003; Zhao et al., 2010). A step further in this application is combining a visible channel with a SWIR channel (i.e., the NDAI from Ciren & Kondragunta (2014) uses the ratio of 0.47μm and 2.13 μm and Qu et al., 2006 uses normalized spectral difference between 2.13 μm and 0.47μm) to maximize the difference in spectral contrasts.

In the IR window region, the different refractive indices of dust in 11μm and 12 μm are used as the basis for brightness temperature difference (BTD) test to distinguish dust from clouds (Shenk & Curran 1974; Wald et al., 1998; Sokolik, 2002; Legrand et al., 2001; Bullard et al., 2008). Both the real and imaginary refractive indices of dust are higher in 11μm than in 12μm, while it is the opposite for an ice cloud. Thus, the difference BTD11μm -12μm is expected to be negative for dust and positive for ice cloud. For the water clouds, the differences in real and imaginary refractive indices are such that they cancel out, leaving BTD11μm -12μm close to zero. Some algorithms use 8.5 μm in addition to 10 μm and 11 μm (tri-spectral) differencing for dust detection (Hu et al., 2008; Ackerman, 1989, 1997; Ashpole & Washington, 2012; Strabala et al., 1994; Hansell et al., 2007; Schepanski et al., 2007). Since brightness temperature not only depends on the optical properties of aerosols, but also on surface emissivity, vertical profiles of atmosphere, aerosol distribution and water vapor, the infrared technique is found to be highly dependent on regions (Hansell et al., 2007).

In addition to single pixel tests, spatial and temporal features of dust have also been used to separate dust from clouds and surface (Jankowiak & Tanré, 1992; Martins et al., 2002; Darmenov & Sokolik, 2009). For example, spatial variability (i.e. pixel-to-pixel) tests in 0.86 μm or 0.64 μm are often used to separate dust from clouds as dust appears more spatially homogenous than clouds. The Infrared differential dust index (IDDI) uses temporal and spatial difference of IR temperature in dusty pixels and clear pixels (Legrand et al., 2001) to detect dust. A summary of dust detection algorithms is

listed in Table 1. Not all of the tests are available for every instrument since each instrument has a limited number of spectral channels.

Since MODIS provides many spectral channels ranging from deep blue, visible to NIR and TIR, there are numerous spectral choices for dust detection. Previous efforts in combining multiple visible and infrared spectral tests have led to many multi-channel dust detection algorithms (e.g., Lee, 1989; Roskovensky & Liou, 2005; Evan et al., 2006; Xie, 2009; Hansell et al., 2007; Zhao et al., 2010; and Cho et al., 2013). Among these, Zhao et al. (2010) is implemented with the standard MODIS cloud mask (MOD35) to detect heavy dust that could potentially be identified as cloud and a dust flag is reported along with other cloud mask tests. The algorithm combines multiple visible and infrared channels and spatial variability in the reflectance at 0.86 μm to detect heavy dust. Initial evaluation of the algorithm shows that the algorithm succeeds in detecting heavy dust plumes near the source regions but misses thin dust far away from source regions (Zhao et al., 2010; Cho et al., 2013). In addition, the algorithm miss identifies many dusty pixels in high latitude oceans.

Dust detection accuracy from major existing algorithms ranges from 60% to 84% depending on regions with false detection rate of about 20% when compared to dust detection from CALIPSO (Ciren & Kondragunta, 2014, Cho et al., 2013). These studies show that current dust detection algorithms could be good at detecting either thick dust, but when faced with thin dust, they allow a large number of false detections.

As an alternative method for MODIS, we might use retrieved parameters from the DT aerosol algorithm (AOD, AE and FMF) to identify pixels that are likely 'dusty'. In general, dust aerosols can be distinguished from background marine aerosol and other pollution and smoke aerosols by their large AOD, small AE and small FMF due to the larger particle sizes, if the retrieval is done correctly. A simple evaluation of the approach is done by comparing the collocated AERONET and MODIS DT retrievals over oceans from all stations in Terra (2000-2014) and Aqua (2002-2014), and applying the same AOD and AE thresholds (AOD>0.5 and AE <0.5) to both AERONET and MODIS DT

retrievals. We find that the AOD retrieval-based dust detection rate is about 67% to 79%. This is not significantly higher than the existing algorithms, and to implement this methodology, it would require an iterative retrieval to apply a dust model.

In summary, dust detection accuracy from major existing algorithms ranges from 60% to 84% with false detection rate of about 20-30% when compared to dust detection from other sensors, including CALIPSO (Ciren & Kondragunta, 2014, Cho et al., 2013). These studies show that current dust detection algorithms have to make a choice between focusing on heavy dust and ignoring thin dust, or accepting large false detection rates in order to identify dust at smaller aerosol loadings. Here we will reevaluate these spectral tests and find a better combination of tests to improve the performance of dust detection for MODIS algorithms.

3.2 Evaluation of dust tests

One of the major difficulties in developing dust detection algorithms is the lack of ground truth. Some algorithms are developed based on a handful of visually selected dusty images (Zhao et al., 2010), while others use retrieved aerosol products such as AOD and AE for dust selection (Ciren & Kondragunta, 2014). The former often fails to represent the diversity of dust properties present across different regions. The latter is sensitive to algorithm deficiencies ranging from inaccurate cloud screening to imperfections in the aerosol models used in the retrieval algorithm.

In this study, we start by carefully assembling a training dataset that has both dusty granules and granules without dust. To represent different scene types, we picked 19 granules which the scene types were visually identifiable, and were from different regions and seasons (Table 2). In addition to dusty scenes, we have included several granules with heavy smoke because separating dust from smoke tends to be a major challenge for both dust and smoke detection algorithms. For each granule, we have manually drawn one or two boxes, and we have grouped the pixels (in 1 km resolution) from these boxes into 5 scene types: dusty, smoky, cloudy, clear over ocean, and

snow/ice surface (Figure 1). The cloud mask from the DT algorithm (based on 3x3 pixel variability and 1.38 mm channel brightness) is used to screen out possible cloud contamination in the smoke and dust samples. This method ensures that the correct scene type is assigned to each 1 km resolution pixel, independent of the retrieved AOD and AE products, which have the potential to be biased.

We then applied spectral tests, including both single channel tests and multi-channel tests to the carefully selected and screened sample pixels. Figure 2 shows probability distribution functions (PDF) of reflectance or brightness temperature from all collected pixels as a function of scene type, for 14 wavelengths commonly used in single channel dust tests. As expected, the clear ocean surfaces have the lowest reflectance in all examined shortwave channels. A quick inspection of the other scene types shows that the reflectance of cloud and snow are generally higher than the dust and smoke scenes in the visible and 0.86 μm channels but the PDFs begin to overlap significantly at wavelengths longer than 1 μm. Among the longwave bands examined, the mid-IR wavelength of 3.9 μm—a region of the spectrum where the brightness temperature signal is dominated by the temperature of the underlying surface and atmosphere—showed the least ability to distinguish the different scene types. The 1.37μm channel is often used to detect thin cirrus clouds because strong water vapor absorption in this region of the spectrum masks radiation from the surface and lower level clouds that could complicate the scene (Gao & Kaufman 1995). The large reflectance seen in this channel for some smoke scenes may be due to rising of smoke to very high altitudes. The cutoff values at 5% and 95% of cumulated PDFs (figures not shown) are listed in Table 3. These values can be used as initial thresholds for each of the tests.

We have identified fifteen tests that combine multiple wavelengths, either as differences, ratios or normalized difference ratios to identify dust. The multi-channel tests (Table 4) manipulate the spectral measurements to minimize the surface's impact on the spectral variations (Figure 3). However, none of the individual multi-channel tests could distinctively separate dust from all other scene types, especially smoke.

A scatter plot of two tests can generally delineate different scene types better as more spectral signals can be used simultaneously to constrain the scenes. We paid special attention to the two indices used in the NOAA's dust detection algorithm (Ciren & Kondragunta, 2014), the dust aerosol index (DAI) and nondust absorbing aerosol index (NDAI):

$$DAI = -100[log_{10}\left(\frac{R_{0.41}}{R_{0.44}}\right) - log_{10}\left(\frac{R'_{0.41}}{R'_{0.44}}\right)] \quad (1)$$

$$NDAI = -10log_{10}\left(\frac{R_{0.41}}{R_{2.13}}\right) \quad (2)$$

Where R is the observed reflectance and R' refers to the reflectance due to Rayleigh scattering. After careful inspection of all one-tests and 2-test combinations, we notice that the DAI test which uses the ratio of two deep blue channels subtract the ratio of reflectance from Rayleigh scattering, is less predictive either by itself or combined with other tests than a single deep blue channel.

However, we find the NDAI to be quite useful when combined with a reflectance test in 0.41 μm (Figure 4a). The 0.41 μm channel is selected to take the advantage of the absorption properties of dust in the deep blue range of the spectrum. This channel has the shortest wavelength of all MODIS channels and separates absorbing dust and smoke from the brighter cloud and snow surface. The NDAI uses the ratio of reflectance at 0.41 μm and 2.13 μm channel to make a distinct separation between the smoke and dust as reported in Ciren & Kondragunta (2014). Because the 2.13 μm channel is very sensitive to particle size (Kaufman et al., 1997) and because dust and smoke are dominated by particles that differ in size by an order of magnitude, reflectance at 2.13 μm has the most promise of separating these two types of aerosol. Thus, by using both 0.41 μm and 2.13 μm, NDAI combines information that should identify aerosol spectral absorption in the shortwave typical of dust and smoke, and then separate the two types of aerosol by size. NDAI alone begins to make that separation, although imperfectly. However, we find that a combination of the 0.41 μm reflectance and NDAI is able to separate dust from most of the other scene types (Figure 4a). We notice the existence of some smoke pixels in

bottom right side of Figure 4a. These smoke pixels come from a thick smoke plume off the Californian coast.

In Figure 4b, the narrow range of dust BTD between 8.7μm and 11μm effectively removes these smoke pixels from dust. In addition to these tests, we also include a spatial variability test in 0.86 μm and reflectance ratio tests in three visible channels (R0.47/R0.65, R0.65/R0.55 and R0.55/R0.47) for initial cloud screening and identifying some particularly heavy dust cases. Our final algorithm combines dust signatures from deep blue, VIS, NIR, SWIR, and TIR spectral regions as follows:

$$\text{9-pixel } stdev(R0.86) < 0.02;$$
$$0.06 < R0.41 < 0.35;$$
$$if \frac{R0.47}{R0.65} < 0.9 \Rightarrow dust;$$
$$if \frac{R0.47}{R0.65} < 0.2 \; then$$
$$if \frac{R0.65}{R0.55} \geq 1.15 \; and \frac{R0.55}{R0.47} \geq 1.15 \Rightarrow dust;$$
$$NDAI > -2.8 \; or$$
$$-10 < NDAI < -2.8 \; and -3.5 < BTD8.6 - 11 < 1.0 \Rightarrow dust;$$

4. Validation of combined dust detection algorithm

4.1 Sample granules

The new dust detection algorithm is tested with the training granules as well as over 50 additional visually identifiable dust and smoke granules. In most cases, the algorithm successfully detects regions of dust in the dusty granules while avoiding misidentifying smoke as dust. In the following, we show a few of such examples. Figure 5 shows dust detections for two heavy dust granules. Under the RGB images, from left to right, we show the dust flags detected with the Zhao et al.(2010) algorithm implemented

within the MODIS cloud mask, the 'likely dust pixels' based on the MODIS DT aerosol retrieval (MxD04) with thresholds set at AOD>0.5 and AE<0.6, and the dust detection flags using the new algorithm. In the first granule, the MYD35 dust algorithm failed to detect the heavy dust over the Red Sea and the Gulf. Meanwhile, the MYD04 dust index indicates most regions as dusty. The new algorithm identifies contiguous regions of dust and non-dust. In the second granule, all three methods identified a heavy dust plume blown off the Australian east coast. The majority of the observed dust appears over the sunglint region in this granule. While the DT algorithm normally does not retrieve in the glint region, it will retrieve dust and assign zero quality confidence if a heavy dust test (R0.47/R0.65<0.95) is satisfied. The new dust detection algorithm also successfully detects the dust even though this particular heavy dust test is not built into the algorithm.

The first granule in Figure 6 shows a large dust and cloud mixed plume over the Atlantic Ocean off the coast of Northwest Africa. In the middle of the granule is a large strip of glint, which prevents the DT algorithm from retrieving any aerosol properties. The new algorithm is able to identify dust pixels continuously from the coast all the way to the western edge of the granule, including over the glint region. The second granule shows two trails of smoke over the South Atlantic Ocean. The AOD and AE criteria confirm that this is not dust, but the Zhao et al. (2010) algorithm mistakenly identifies some pixels as dusty. The new dust algorithm successfully avoided this misidentification.

4.2 AERONET dust pixels

For a more quantitative evaluation of the new dust detection algorithm, we compare with AERONET. The dust detection algorithm is applied to ocean MODIS pixels collocated spatially and temporally with AERONET measurements, as described in Section 2. One year of data is analyzed, 2011, which consists of 44900 and 45551 10-km pixels from Aqua-AERONET and Terra-AERONET collocations, respectively. The collocation uses the 10-km MxD04 output, but the dust detection algorithm uses reflectance and brightness temperature inputs at 1 km resolution. Therefore, for each 10-km aerosol retrieval pixel, we go back to the MxD02 in order to input the corresponding

10x10 1-km L1B reflectance and BT data and apply the dust detection tests to each of these 1-km pixels. We consider the entire 10-km retrieval pixel as dusty if at least 3 1-km pixels are identified as dusty by the new dust detection algorithm.

Thresholds have to be set to determine dust in the AERONET observations. Because we want to understand how our dust detection algorithm works across a range of aerosol loadings, unlike previous validations of such algorithms, we introduce a set of dynamic thresholds for AERONET pixels from weakest to strongest loadings:

$$\begin{Bmatrix} AOD \\ AE \end{Bmatrix} \begin{matrix} \geq \\ \leq \end{matrix} \left\{ \begin{pmatrix} 0.3 \\ 0.8 \end{pmatrix}; \begin{pmatrix} 0.4 \\ 0.7 \end{pmatrix}; \begin{pmatrix} 0.5 \\ 0.6 \end{pmatrix}; \begin{pmatrix} 0.6 \\ 0.5 \end{pmatrix}; \begin{pmatrix} 0.7 \\ 0.4 \end{pmatrix}; \begin{pmatrix} 0.8 \\ 0.4 \end{pmatrix} \right\}$$

As the aerosol loading increases, we demand AE to decrease for the observation or scene to be declared dusty. This assumes the background aerosol to consist of more fine mode aerosol and increasing aerosol loading is due to more coarse mode dust.

To provide more quantitative match up statistics, we computed the accuracy, probability of correct detection (POCD) and probability of false detection rate (POFD) assuming AERONET dust detection as truth. Successful retrievals consist of TP (True Positive) and TN (True Negative) cases, in which both algorithms identify the pixel as dusty and no dust, respectively, and unsuccessful retrievals consist of FN (False Negative) and FP (False Positive) – where the new algorithm identifies a pixel as no dust and dust respectively, opposite to what AERONET defines.

$$Accuracy = \frac{TP + TN}{TP + TN + FN + FP} \times 100\% \quad (3)$$

$$POCD = \frac{TP}{TP + FN} \times 100\% \quad (4)$$

$$POFD = \frac{FP}{TN + FP} \times 100\% \quad (5)$$

The POCD and POFD here depend on the AERONET dust criteria (Fig. 7a, c). For example, if a weak criterion is used, i.e., AOD > 0.3 and AE < 0.8, more dusty pixels would be identified by AERONET and the new dust detection reports a low 27% and 30% of POCD from collocated Aqua and Terra dataset, respectively. If a strong criterion is used, i.e., AERONET AOD > 0.6 and AE < 0.5, the POCD from the new algorithm is more than 90% and 82% for Aqua and Terra, respectively. For a commonly used threshold criterion with AOD > 0.5 and AE < 0.6 (Ciren & Kondragunta 2014), POCD is about 70%.

The POFD in all cases are low, varying from 0.6% to 1.3% from weakest to strongest AERONET criteria due to the large number of TN pixels (Fig. 7b, 7d). For comparison, we plotted POCD and POFD if an alternative dust detection method is used with DT retrieved AOD and AE (i.e., AOD > 0.5 and AE < 0.6). The new algorithm detects 1.5 to 3 times more dusty pixels with only an insignificant increase in false positives than would the old standard DT algorithm as the first step in an iterative procedure.

4.3 Dust Validation with CALIPSO aerosol layer type

The aerosol layer feature from CALIOP has been used as benchmark for many dust detection algorithms (Ciren & Kondragunta, 2014). Here we used a 5-km CALIOP aerosol layer product collocated with a MODIS Aqua product from January, April, July and October 2010. Only pixels with no cloud layers are selected. Again, the new algorithm is applied to 10x10 1-km pixels centered at the CALIOP pixel. The MODIS 10-km pixel is defined as dusty if more than 3 1-km pixels are classified as dusty. The CALIOP aerosol layer has up to 8 aerosol layers, and dust-related aerosol layers can be denoted as ‘dust’, ‘polluted dust’ or ‘marine dust’. For a CALIOP horizontal pixel to be classified as dusty in a total column sense for comparison with MODIS, we require the AOD from 532nm CALIOP backscattering AOD retrieval to be greater than 0.3 and vary the number of required pure dust layers. The dust detection validation statistics are computed as a function of the number of required dust layers. We did not include marine

dust and polluted dust because optical properties of these dust are different than pure dust (in the CALIPSO detection algorithm).

Figure 8 shows the dusty pixel counts in 1° x 1° grid boxes when requiring different number of minimum dust layers in the CALIOP data: for a minimum of 1 dust-layer (Fig.8a) or 3 dust-layers (Fig. 8b). The corresponding MODIS dusty pixel counts from the new dust detection algorithm is shown in Fig. 8c. Requiring only one dust-layer leads to many more identified dusty pixels than requiring three or more dust layers. In fact, CALIOP 1-dust-layer detections could appear anywhere on the globe, unless also accompanied by backscatter AOD restrictions (figure not shown). Hence, requiring more dusty layers is necessary to guarantee enough dust in the column to merit a revised MODIS retrieval. The new dust algorithm shows similar regional distributions as the 3-dust-layer case, albeit the total number is still less than the 3-dust-layer case.

Table 5 shows the match metrics for dusty pixels defined using different number of dust layers, respectively. With 1-dust-layer as the dusty criteria for CALIOP, the new algorithm's POCD is only 30.7%. As the number of dust layers increases, POCD increases. The POCD is 40.2% and 74.6% for 3-dust-layer and 5-dust-layer criteria, respectively. In all cases, the POFD is less than 1%. Since our purpose of dust detection is to identify pixels for the aerosol retrieval algorithm to confidently assign a non-spherical dust model, our new dust algorithm serves this purpose. It captures the heavy dusty pixels while the false classification rate is extremely low.

5. Global dusty pixel distribution

The dust detection algorithm is applied globally to Aqua MODIS from Apr. 12 to May 11, 2011 (Figure 9) and July 1 to July 31, 2011 (Figure 10). The two periods are selected to capture dust prevalence in northwest Asia in April (spread over Northwest Pacific, Yu et al., 2012) and the heaviest period of Africa dust occurring in July (Huang et al., 2010). Figure 9 shows that MxD35 dust flag captures many dusty pixels in the northwest Pacific and a small amount of the dusty pixels in north Atlantic off west

Africa. But there are a lot of miss identified dusty pixels in the high latitude Southern Ocean and North Atlantic. Using the DT-retrieved AOD and AE values for dusty identification identifies only a few dusty pixels in subtropical North Atlantic, Mediterranean, Persian Gulf and Northwest Pacific regions. The new dust algorithm returns more dusty pixels across north Atlantic, Mediterranean, Persian Gulf and northwest Pacific. The small number of dusty pixels across the north Pacific may be transported dust from east Asia. Interestingly, all detection algorithms find dusty pixels in the north Atlantic off New England. With no obvious sources of dust, this is likely a case where turbid water and/or fog may be causing false dust detection.

For July 2011, we notice that the new dust algorithm detects more dust pixels over the subtropical north Atlantic, Mediterranean, Persian Gulf, and especially the Arabian Sea, but fewer dust pixels off east Asia. This appears to match the expected seasonal variation of dust events in these regions (Voss and Evan, 2020). Compared with dust detection from the MxD35 dust flag and the AOD- AE-based dust flag, the new dust detection algorithm captures more of the heavy dusty pixels, and reduces false dust detection in the southern oceans.

6. Summary and discussion

The Dark-target (DT) aerosol retrieval is an operational algorithm of the MODIS instruments that retrieves spectral aerosol optical depth (AOD) over land and ocean. Over the ocean, the DT algorithm is known to produce biased retrievals of AOD, AE, and FMF, in pixels containing significant dust aerosol because the current version of DT-O does not have an aerosol model capable of faithfully representing these non-spherical dust particles. In this work, we designed and evaluated a two-step dust aerosol retrieval strategy in which we first detect dust pixels and then utilize a new non-spherical dust model in the retrieval of the detected dusty pixels. Here, in Part I of the series, we reported on a dust detection algorithm that combines near-UV (deep blue), visible, and thermal infrared (TIR) wavelength spectral tests based on a survey of existing dust detection algorithms.

The new dust detection algorithm was tested extensively with manually selected dusty granules. Quantitative evaluation of the dust detection algorithm is conducted with collocated AERONET-MODIS detections as well as CALIPSO – MODIS collocations. Instead of using one set of arbitrary threshold criteria, we used progressively changing criteria from weakest to strongest aerosol loading so that the full nature of the dust detection algorithm could be evaluated, from detecting weakly to heavy dust situations. From comparison with both AERONET and CALIOP products, we estimate the new dust detection algorithm detects about 30% of dusty pixels in weak aerosol loading and above 80% of heavy dust pixels. Compared with the dust flag currently implemented inMxD35, and a dust classification scheme based on commonly used thresholds with AOD and AE, the new dust detection algorithm finds more dusty pixels with much fewer false dust detections over high-latitude oceans.

We should point out that the dust detection algorithm developed in this work is not comprehensive due to the extreme complexity of dust's varying physical sizes and chemical compositions in any given region and time. Even though our searching for dust detection tests is guided by physical principals, our method still relies on manually tuning the thresholds which is very difficult for decision trees that involve many layers of nonlinear processes. We expect that a machine learning algorithm might be able to determine better thresholds and an improved decision procedure (Wang et al., 2019). Such work is underway, however, it is guided by the knowledge accumulated through physical-based experiment and discovery. The impact of the dust detection scheme developed and reported here on aerosol retrievals in the DT algorithm will be explored in Part II of the series as we describe the development and testing of new dust aerosol models for the algorithm.

Although Terra and Aqua will be out of orbit in a few years after providing nearly two decades of high-quality observations, the DT algorithms have recently been ported to the VIIRS instruments onboard the Suomi-NPP because of their similar orbital and spectral characteristics as MODIS (Sawyer et al., 2019). In addition, the DT algorithm is

being adapted to the next generation geostationary satellites such as the Advanced Baseline Imager (ABI) on GOES-East and GOES-West and the Advanced Himawari Imager (AHI) on Himawari (Gupta et al., 2019). The dust detection algorithm developed for MODIS would require slight adjustments of thresholds for the VIIRS instrument because of its slightly different spatial resolution and spectral channels than the MODIS and possibly more substantial adjustments for the ABI and AHI instruments because their lack of deep blue channels. It is important to implement a proper non-spherical dust model in the DT-O retrieval algorithm to provide better quality dusty retrievals for both climate studies and air quality monitoring.

Acknowledgement: This work is supported by NASA NNH13ZDA001NTERAQEA and DSCOVR Earth Science Algorithms managed by Richard Eckman. The authors would like to thank Richard G. Kleidman and Santiago Gassó for providing sample dusty granules, William R. Espinosa and Santiago Gassó for helpful comments on the manuscript. MODIS level 1 (MxD02) and level 2 (MxD04, MxD35) data are available from NASA DAAC. AERONET products can be obtained from AERONET website (https://aeronet.gsfc.nasa.gov).The CALIPSO Level 2 Cloud/Aerosol layer products (version 4) products are publicly available from the Atmospheric Science Data Center (https://eosweb.larc.nasa.gov/).

References

Ackerman, S. A. (1989). Using the radiative temperature difference at 3, 7 and 11 μm to track dust outbreaks. Remote Sens. Environ. 27, 129–133.

Ackerman, S. A. (1997). Remote sensing aerosols using satellite infrared observations. J. Geophys. Res., 102(D14), 17069–17079, doi:10.1029/96JD03066.

Ahmad, Z., & R. S. Fraser (1982). An Iterative Radiative Transfer Code For Ocean-Atmosphere Systems, J. Atmos. Sci., 39, 656–665, https://doi.org/10.1175/1520-0469(1982)039<0656:AIRTCF>2.0.CO;2.

Ashpole, I., & Washington, R. (2012). An automated dust detection using SEVIRI: A multiyear climatology of summertime dustiness in the central and western Sahara, J. Geophys. Res., 117, D08202, doi:10.1029/2011JD016845.

Bullard, J. E., Baddock, M. C., McTainsh, G. H., & Leys, J. F. (2008). Sub-basin scale dust source geomorphology detected using MODIS, Geophys. Res. Lett., 35, L15404, doi:10.1029/2008GL033928.

Chou, C., Formenti, P., Maille, M., Ausset, P., Helas, G., Harrison, & M., Osborne, S. (2008). Size distribution, shape, and composition of mineral dust aerosols collected during the African Monsoon Multidisciplinary Analysis Special Observation Period 0: Dust and Biomass-Burning Experiment field campaign in Niger, January 2006. J. Geophys. Res. Atmos., 113 (D23).

Ciren, P., & Kondragunta, S. (2014). Dust aerosol index (DAI) algorithm for MODIS, J. Geophys. Res. Atmos., 119, 47704792, doi:10.1002/2013JD020855

Darmenov, A., & Sokolik, I. N. (2005). Identifying the regional thermal-IR radiative signature of mineral dust with MODIS, *Geophys. Res. Lett.*, 32, L16803, doi:10.1029/2005GL023092.

Darmenov, A., & Sokolik, I.N. (2009). Spatial variability of satellite visible radiances in dust and dust-cloud mixed conditions: Implications for dust detection, Geophys. Res. Lett., 36, L14811, doi:10.1029/2009GL038383.

Dubovik, O., & King, M.D. (2000). A flexible inversion algorithm for retrieval of aerosol optical properties from Sun and sky radiance measurements. J. Geophys. Res., 105, 20 673-20 696.

Dubovik, O., Holben, B., Eck, T.F., Smirnov, A., Kaufman, Y.J., King, M.D., Tanré, D., & Slutsker, I. (2002). Variability of absorption and optical properties of key aerosol types observed in worldwide locations. Journal of the atmospheric sciences, 59(3), pp.590-608.

Dubovik, O., Herman, M., Holdak, Lapyonok, T., Tanré, D., Deuzé, J. L., Ducos, F. Sinyuk, A., and Lopatin, A. (2011), Statistically optimized inversion algorithm for en- hanced retrieval of aerosol properties from spectral multi-angle polarimetric satel- lite observations, Atmospheric Measurement Techniques, 4(5), 975–1018, doi:10.5194/ amt-4-975-2011.

Eck, T. F., Holben, B. N., Reid, J. S., Dubovik, O., Smirnov, A., O'Neill, N. T., Slutsker, I., & Kinne, S. (1999). Wavelength dependence of the optical depth of biomass burning, urban, and desert dust aerosols, J. Geophys. Res.-Atmos., 104, 31333–31349, https://doi.org/10.1029/1999JD900923.

Evans, K. F., & Stephens, G. L. (1991). A new polarized atmospheric radiative transfer model, J. Quant. Spectrosc. Ra., 46, 413–42.

Evan, A. T., Heidinger, A. K., & Pavolonis, M. J. (2006). Development of a new over-water advanced very high resolution radiometer dust detection algorithm, Int. J. Remote Sens., 27, 3903–3924, doi:10.1080/01431160600646359.

Gaiero, D., Gassó, S., Simonella, L., & Stein. A. F., (2013). Ground/satellite observations and atmospheric modeling of dust storms originating in the high Puna-Altiplano deserts (South America): Implications for the interpretation of paleo-climatic archives. J. Geophys. Res. Atmos. 118 (9): 3817–3831 [10.1002/jgrd.50036]

Gao, B. C., & Y. J. Kaufman, Y.J. (1995). Selection of the 1.375 /am MODIS channel for remote sensing of cirrus cloudsand stratospheric aero- sols from space, J. Atmos. Sci., 52, 4231-4237.

Gassó, S., Stein, A., Marino, F. et al., (2010). A combined observational and modeling approach to study modern dust transport from the Patagonia desert to East Antarctica. Atmos. Chem. Phys. 10 (17): 8287-8303 [10.5194/acp-10-8287-2010]

Giles, D. M., Sinyuk, A., Sorokin, M. G., Schafer, J. S., Smirnov, A., Slutsker, I., Eck, T. F., Holben, B. N., Lewis, J. R., Campbell, J. R., Welton, E. J., Korkin, S. V., & Lyapustin, A. I.(2019). Advancements in the Aerosol Robotic Network (AERONET)

Version 3 database – automated near-real-time quality control algorithm with improved cloud screening for Sun photometer aerosol optical depth (AOD) measurements, Atmos. Meas. Tech., 12, 169–209, https://doi.org/10.5194/amt-12-169-2019.

Goudie, A.S., & Middleton, N.J. (2006) Desert Dust in the Global System. Springer.

Goudie, A.S., Deseart dust and human health disorders. Envion. Int., 63, 101-103, doi:10.1016/j.envint.2013.10.011.

Griffin, D. W. (2007). Atmospheric Movement of Microorganisms in Clouds of Desert Dust and Implications for Human Health, Clinical Microbiology Reviews. 20 (3): 459–77, doi:10.1128/CMR.00039-06.

Gupta, P., Levy, R. C., Mattoo, S., Remer, L. A., Holz, R. E., & Heidinger, A. K. (2019). Applying the Dark Target aerosol algorithm with Advanced Himawari Imager observations during the KORUS-AQ field campaign, Atmos. Meas. Tech., 12, 6557–6577, https://doi.org/10.5194/amt-12-6557-2019.

Hansell R. A., Ou, S.C., Liou, K.N., Roskovensky, J. K., Tsay, S.C., Hsu, C., & Ji, Q. (2007). Simultaneous detection/separation of mineral dust and cirrus clouds using MODIS thermal infrared window data, Geophys. Res. Lett., 34, L13802, doi:10.1029/2007GL031035.

Harrison, S.P., Kohfeld, K.E., Roelandt, C. , & Claquin, T. (2001). The role of dust in climate changes today, at the last glacial maximum and in the future. Earth-Science Reviews, 54(1), pp.43-80.

Hao, X., & Qu, J. J. (2007), Saharan dust storm detection using Moderate Resolution Imaging Spectroradiometer thermal infrared bands. J. Appl. Remote Sens., 1, 013510, doi:10.1117/1.2740039.

Herman, J. R., Bhartia, P. K., Torres, O., Hsu, N.C., Seftor, C. J., & Celarier, E. (1997). Global distribution of UV-absorbing aerosols from Nimbus 7/TOMS data, J. Geophys. Res., 102(D14), 16,911–16,921.

Holben, B. N. (1998). AERONET—A federated instrument network and data archive for aerosol characterization, Remote Sens. Environ., 66, 1–16.

Hsu, N.-Y. C., Tsay, S.-C., King, M. D., &. J. R. (2004). Aerosol properties over bright-reflecting source regions. IEEE Trans Geosci Remote Sens, 42 (3): 557-569 [10.1109/TGRS.2004.824067]

Hsu, N. C., Tsay, S. -C., King, M. D., & Herman, J. R. (2006). Deep blue retrievals of Asian aerosol properties during ACE-Asia, IEEE Trans. Geosci. Remote Sens., 44(11), 3180–3195, doi:10.1109/TGRS.2006.879540.

Hsu, N. C., Lee, J., Sayer, A.M. , et al., (2019). VIIRS Deep Blue Aerosol Products Over Land: Extending the EOS Long-Term Aerosol Data Records. *Journal of Geophysical Research: Atmospheres* **124** (**7**): 4026-4053

Hu, X. Q., Lu, N. M., Niu, T., & Zhang, P. (2008). Operational retrieval of Asian sand and dust storm from FY-2C geostationary meteorological satellite and its application to real time forecast in Asia, Atmos. Chem. Phys., 8, 1649–1659.

Huang, J., Zhang, C., & Prospero, J. M. (2010). African dust outbreaks: A satellite perspective of temporal and spatial variability over the tropical Atlantic Ocean, J. Geophys. Res., 115, D05202, doi:10.1029/2009JD012516.

Jankowiak, I., & Tanré, D. (1992). Satellite climatology of Saharan dust outbreaks: Method and preliminary results, J. Clim., 5, 646–656.

Kaufman, Y. J., Tanré, D., Remer, L., Vermote, E., Chu, A., & Holben, B.N. (1997). Remote sensing of tropospheric aerosol from EOS-MODIS over the land using dark targets and dynamic aerosol models, J. Geophys. Res., 102(D14), 17,051–17,067.

Kaufman, Y. J., Tanré, D., Remer, L. A., Vermote, E.F., Chu, A., & Holben, B.N. (1997). Operational remote sensing of tropospheric aerosol over land from EOS moderate resolution imaging spectroradiometer, J. Geophys. Res., 102(D14), 17051–17067, doi:10.1029/96JD03988.

Kaufman, Y. J., Karnieli, A. & Tanré, D. (2000). Detection of dust over deserts using satellite data in the solar wavelengths, IEEE Geosci. Remote Sens., 38(1), 525–531.

Kaufman, Y. J., Tanre, D. & Boucher, O. (2002). A satellite view of aerosols in the climate system, Nature, 419, 215–223.

Kaufman, Y. J., Koren, I., Remer, L. A., Tanré, D., Ginoux, P., & Fan, S. (2005). Dust transport and deposition observed from the Terra-Moderate

Resolution Imaging Spectroradiometer (MODIS) spacecraft over the Atlantic Ocean, J. Geophys. Res., 110, D10S12, doi:10.1029/2003JD004436.

Kim, D., et al. (2014). Sources, sinks, and transatlantic transport of North African dust aerosol: A multimodel analysis and comparison with remote sensing data, J. Geophys. Res. Atmos., 119, 6259– 6277, doi:10.1002/2013JD021099.

Kok, J. F., Ward, D.S., Mahowald, N.M., & Evan, A.T. (2018). Global and regional importance of the direct dust-climate feedback, *Nature Communications*, 9, 241.

Lee, T. F. (1989). Dust tracking using composite visible/IR images: A case study, Weath. Forecast., 4, 258–262.

Legrand, M., Nertrand, J. J., Desbois, M., Menenger, L., & Y. Fouquart, Y. (1989). The potential of infrared satellite data for the retrieval of Saharan dust optical depth over Africa. J. Climate Appl. Meteor., 28, 309–318.

Legrand, M., Plana-Fattori, A., & N'doume, C. (2001). Satellite detection of dust using the IR imagery of Meteosat: 1. Infrared differences dust index, J. Geophys. Res., 106(D16), 18,251–18,274.

Levy, R.C., Remer, L.A., & Dubovik, O. (2007a). Global aerosol optical properties and application to Moderate Resolution Imaging Spectroradiometer aerosol retrieval over land. Journal of Geophysical Research: Atmospheres, 112(D13).

Levy, R.C., Remer, L.A., Mattoo, S., Vermote, E.F., & Kaufman, Y.J., (2007b). Second-generation operational algorithm: Retrieval of aerosol properties over land from inversion of Moderate Resolution Imaging Spectroradiometer spectral reflectance. Journal of Geophysical Research: Atmospheres, 112(D13).

Levy, R. C., Remer, L. A., Kleidman, R. G., et al., (2010). Global evaluation of the Collection 5 MODIS dark-target aerosol products over land. Atmos. Chem. Phys., 10 (21): 10399-10420 [10.5194/acp-10-10399-2010]

Levy, R.C., Mattoo, S., Munchak, L.A., Remer, L.A., Sayer, A.M., Patadia, F., & Hsu, N.C. (2013). The collection 6 modis aerosol products over land and ocean. Atmos. Meas. Tech., 6, 2989–3034.

Lyapustin, A., Wang, Y., Korkin,S., & Huang, D. (2018). MODIS Collection 6 MAIAC algorithm. *Atmospheric Measurement Techniques* **11** (**10**): 5741-5765 [10.5194/amt-11-5741-2018]

Martins, J. V., Tanré, D., Remer, L., Kaufman, Y., Mattoo, S. & R. Levy, R. (2002). MODIS Cloud screening for remote sensing of aerosol over oceans using spatial variability, Geophys. Res. Lett., 29(12), 1619, doi:10.1029/2001GL013252.

Miller, R.L., & Tegen, I. (1998). Climate response to soil dust aerosols. J. Climate, 11, 3247-3267, doi:10.1175/1520-0442(1998)011<3247:CRTSDA>2.0.CO;2.

Miller, S. D. (2003). A consolidated technique for enhancing desert dust storms with MODIS, Geophys. Res. Lett., 30(20), 2071, doi:10.1029/2003GL018279.

Prospero, J. M., & Lamb, P.J. (2003). African droughts and dust transport to the Caribbean: Climate change implications, Science, 302, 1024–1027.

Prospero, J. M., Collard, F.-X., Molinié, J., & Jeannot, A. (2014). Characterizing the annual cycle of African dust transport to the Caribbean Basin and South America and its impact on the environment and air quality, Global Biogeochem. Cycles, 29, 757– 773, doi:10.1002/2013GB004802.

Qu, J. J., Hao, X., Kafatos, M. &Wang, L. (2006). Asian dust storm monitoring combining Terra and Aqua MODIS SRB mea- surements. IEEE Geosci. Remote Sens. Lett., 3, 484–486.

Remer, L. A., & Coauthors, (2005). The MODIS aerosol algorithm, products, and validation. J. Atmos. Sci., 62, 947–973.

Rosenfeld, D., Clavner,M., & Nirel,R. (2011), Pollution and dust aerosols modulating tropical cyclones intensities, Atmospheric Research,102, 66-76, doi.org/10.1016/j.atmosres.2011.06.006.

Roskovensky, J. K., & Liou, K.N. (2005). Differentiating airborne dust from cirrus clouds using MODIS data. Geophys. Res. Lett., 32, L12809, doi:10.1029/2005GL022798.

Sawyer, V.; Levy, R.C.; Mattoo, S.; Cureton, G.; Shi, Y.; Remer, L.A. Continuing the MODIS Dark Target Aerosol Time Series with VIIRS. *Remote Sens.* **2020**, *12*.

Schepanski, K., Tegen, I. Laurent, B. Heinold, B. & Macke, A. (2007). A new Saharan dust source activation frequency map derived from MSG–SEVIRI IR-channels, Geophys. Res. Lett., 34, L18803, doi:10.1029/2007GL030168.

Shell, K. M., & Somerville, R.C.J. (2007). Sensitivity of climate forcing and response to dust optical properties in an idealized model, J. Geophys. Res., 112, D03206, doi:10.1029/2006JD007198.

Shenk, W. E., &Curran, R.J. (1974), The detection of dust storms over land and water with satellite visible and infrared measurements, Mon. Wea. Rev., 102, 830–837.

Shi, Y. R., Levy, R. C. Eck, T.F., et al., 2019. Characterizing the 2015 Indonesia fire event using modified MODIS aerosol retrievals. Atmospheric Chemistry and Physics, 19 (1): 259-274 [10.5194/acp-19-259-2019]

Sokolik, I. N. (2002). The spectral radiative signature of wind-blown mineral dust: Implications for remote sensing in the thermal IR region, Geophys. Res. Lett., 29(24), 2154, doi:10.1029/2002GL015910.

Strabala, K. I., Ackerman, S.A., & Menzel, W. P. (1994). Cloud properties inferred from 8–12 mm data, J. Appl. Meteorol., 33, 212–229.

Tanré, D., & Legrand, M. (1991). On the satellite retrieval of Saharan dust optical thickness over land: Two different approaches, J. Geophys. Res., 96(D3), 5221–5227, doi:10.1029/90JD02607.

Tanré, D., Kaufman, Y. .J., Herman, M., & Mattoo, S. (1997). Remote sensing of aerosol properties over oceans using the MODIS/EOS spectral radiances. J. Geophys. Res., 102, (D14),. 16971–16988.

Torres, O., Bhartia, P., Herman, J. R., Ahmad, Z., &. J.F. (1998). Derivation of aerosol properties from satellite measurements of backscattered ultraviolet radiation. Theoretical basis. J Geophys Res, 103 (D14): 17099-17110 [10.1029/98JD00900]

Torres, O., A. Tanskanen, B. Veihelman, et al., (2007). Aerosols and Surface UV Products from OMI Observations: An Overview. J. Geophys. Res., 112 (D24): D24S47 [10.1029/2007JD008809].

Verge-Depre, G., Legrand, M., Moulin, C., Alias, A., Francois, P. (2006). Improvement of the detection of desert dust over the Sahel using METEOSAT IR imagery. Ann. Geophys. , 24, 2065–2073.

Voss, K.K., & Evan, A.T. (2020). A New Satellite-Based Global Climatology of Dust Aerosol Optical Depth. *J. Appl. Meteor. Climatol.,* **59**, 83–102,https://doi.org/10.1175/JAMC-D-19-0194.1

Wald, A. E., Kaufman, Y.J., Tanré, D. & Gao, B.-C. (1998). Daytime and nighttime detection of mineral dust over desert using infrared spectral contrast, J. Geophys. Res., 103, 32,307–32,313.

Wang, C., Platnick, S., Meyer, K., Zhang, Z., and Zhou, Y. (2019). A Machine Learning-Based Cloud Detection and Thermodynamic Phase Classification Algorithm using Passive Spectral Observations, Atmos. Meas. Tech. Discuss., https://doi.org/10.5194/amt-2019-409, in review.

Weinzierl, B., & Coauthors, (2012). On the visibility of airborne volcanic ash and mineral dust from the pilot's perspective in flight. Phys. Chem. Earth, 45–46, 87–102, doi:https://doi.org/10.1016/j.pce.2012.04.003.

Winker, D. M., Tackett, J. L., Getzewich, B.J., Liu, Z., Vaughan, M. A. & Rogers, R. R. (2013). The global 3-D distribution of tropospheric aerosols as characterized by CALIOP. *Atmos. Chem. Phys.*, **13,** 3345-3361, doi:10.5194/acp-13-3345-2013.

Wiscombe, W. J. (1980). Improved Mie scattering algorithms, Appl. Optics, 19, 1505–1509, https://doi.org/10.1364/AO.19.001505.

Wyser, K. (1998). The effective radius in ice clouds. *Journal of Climate.* 11, 7, 1793-1802.

Yu, H., et al., (2006), A review of measurement based assessments of the aerosol direct radiative effect and forcing, Atmos. Chem. Phys., 6, 613–656.

Yu, H., Remer, L.A., Kahn, R. A., Chin, M., Zhang, Y. (2012). Satellite perspective of aerosol intercontinental transport: From qualitative tracking to quantitative characterization Atmospheric Research, 124 (2013), pp. 73-100, 10.1016/j.atmosres.2012.12.013.

Yu, H., et al., (2006), A review of measurement based assessments of the aerosol direct radiative effect and forcing, Atmos. Chem. Phys., 6, 613–656.

Zhao, C., Liu, X., Leung, L. R., & S. Hagos, S. (2011). Radiative impact of mineral dust on monsoon precipitation variability over West Africa, Atmos. Chem. Phys., 11, 1879–1893, doi:10.5194/acp-11-1879-2011.

Zhao, T. X.-P., Ackerman, S., & Guo, W. (2010), Dust and smoke detection for multi-channel imagers, Remote Sens., 2, 2347–2368, doi:10.3390/rs2102347.

Table 1: Review of plausible dust optical properties from previous works.

Names	Tests	References
IR split window	BTD11 μm - 12 μm; BTD8.7 μm -11 μm	Shenk and Curran 1974; Strabala et al., 1994; Ackerman 1989, 1997; Legrand et al., 1989, 2001; Wald et al., 1998; Legrand et al., 2001; Sokolik, 2002; Darmenov & Sokolik 2005; Roskovensky & Liou, 2005; Evan et al., 2006; Schepanski et al., 2007; Hao & Qu 2007; Hansell et al., 2007; Hu et al., 2008; Bullard et al., 2008; Ashpole & Washington, 2012
SWIR	3.76 μm; 3.76 μm -11μm	Legrand et al., 2001;
NIR	1.64um, 2.13 μm	Qu et al., 2006; Ciren & Kondragunta, 2014
Visible	ρ at 0.47μm, 0.55 μm, 0.67μm, 0.86μm; 2-channel ratio: ρ_1/ρ_2; Normalized difference ratio: $(\rho_1-\rho_2)/(\rho_1+\rho_2)$	Tanré & Legrand 1991; Kaufman et al., 2000; Miller 2003; Qu et al., 2006; Jankowiak & Tanré, 1992; Zhao et al., 2010

Deep blue, UV	-10*[Log (ρ0.41/ρ0.47) -log(ρ0.41/ρ0.47)$_r$); -10*[Log (ρ0.41/ρ0.44) -log(ρ0.41/ρ0.44)$_r$)	Herman et al., 1997; Torres et al., 1998, 2007; Hsu et al., 2004; Ciren & Kondragunta, 2014
Spatial variability Spatial/temporal contrast with clear sky	ρ at 0.87μm, 0.64 μm	Tanré & Legrand, 1991 Jankowiak & Tanré,1992; Martins et al., 2002 Darmenov & Sokolik, 2009

Table 2: Training granules for dust detection.

Satellite	Granule (year, day, hhmm)	Location	Scene
Aqua	2009,196,1015	Red Sea and Persian Gulf	Dust over ocean
Aqua	2014,113,1110	Mediterranean	dust over ocean
Aqua	2014,162,1505	Off west Africa	dust over ocean
Aqua	2010,048,1150	Mediterranean	dust over ocean thin
Aqua	2013,053,1115	Mediterranean	mixed over ocean
Aqua	2015,032,1135	Mediterranean	dust over ocean
Terra	2009,188,0750	Persian Gulf	thick dust over ocean
Terra	2009,266,0005	Off East Australia	dust storm
Terra	2009,115,0300	Southeast China	Dust mixed with cloud
Aqua	2013,018,0550	Northern China Sea	Dust

Aqua	2011,131,0515	Northern China Sea	Dust
Aqua	2007,296,2140	Coast off California	Smoke
Aqua	2011,157,1525	South Atlantic Ocean	smoke over ocean
Terra	2003,301,1825	Off California coast	Smoke over ocean
Aqua	2015,115,0720	Arctic	Snow surface
Aqua	2011,157,1345	South Atlantic Ocean	cloud over ocean clear ocean
Terra	2009,115,0300	Southern	China dust blown from west to sea
Aqua	2018,030,1850	South Atlantic Ocean	Dust blown off Patagonia
Terra	2017,318,2115	Gulf of Alaska	Dust blown off Alaska

Table 3. Single channel tests and cutoff values at 5% and 95% accumulated PDF. "R" means 'reflectance', and "BT" means brightness temperature.

MODIS Channel	Wavelength	Dusty range
M08	R0.41	[0.20, 0.29]
M09	R0.44	[0.18, 0.29]
M03	R0.47	[0.17, 0.29]
M04	R0.55	[0.13, 0.34]
M01	R0.65	[0.10, 0.39]
M02	R0.86	[0.08, 0.44]
M05	R1.26	[0.06, 0.42]
M26	R1.37	<0.03 for all cases
M07	R2.13	[0.03, 0.35]
M20	BT3.7	[292.5, 314.3]
M21	BT3.9	[287.0, 303.2]

M29	BT8.7	[279.5, 296.2]
M31	BT11	[279.0, 298.4]
M32	BT12	[280.1, 298.2]

Table 4. Multi-channel tests and cutoff values at 5% and 95% accumulated PDF.

	Test	Dusty range
1	BT11-12	[-1.34, 0.48]
2	BT11-3.7 or (BT3.9-11)	[-31.5, -6.51]
3	BT8.7-11	[-3.16, -0.01]
4	R0.55/R0.47	[0.72, 1.17]
5	R0.65/R0.55	[0.80, 1.16]
6	R0.47/R0.65	[0.63, 1.54]
7	NDSI snow index (R0.65-R2.13)/(R0.65+R2.13);	[-0.0, 0.39]
8	NDDI (R2.13-R.47)/(R2.13+R0.47)	[-0.64, 0.09]
9	NDVI (R0.86-R0.65)/(R0.86+R0.65)	[-0.12, 0.28]
10	SNDVI (R0.47-R0.65)/(R0.47+R0.65)	[-0.20, 0.20]
11	DAI (R0.412/R0.440)	[6.24, 14.05]
12	NDAI (R0.410/R2.110)	[-7.33, 0.77]
13	B8-7-1 slope (R0.41-R2.13)/(R0.65-R0.41)	[-11.80, 4.33]
14	SFCDIF (SST-BT11)	[0.26, 6.5]
15	STDEV (0.86 μm)	[-0.02, 0.01]

Table 5. Dust detection statistics based on MODIS-AQUA and CALIPSO collocated pixels from April and July 2010. Total number of non-cloudy pixels based on CALIOP is 1261460.

No. CALIPSO Pure Dust Layers	No. CALIPSO Dusty Pixels	Accuracy	POCD	POFD
1	23458	98.6	30.7	0.2
2	16889	98.9	34.7	0.3
3	7018	99.2	40.2	0.5
4	1708	99.3	50.3	0.7
5	327	99.3	74.6	0.7
6	65	99.3	96.9	0.7
7	5	99.3	100.0	0.7

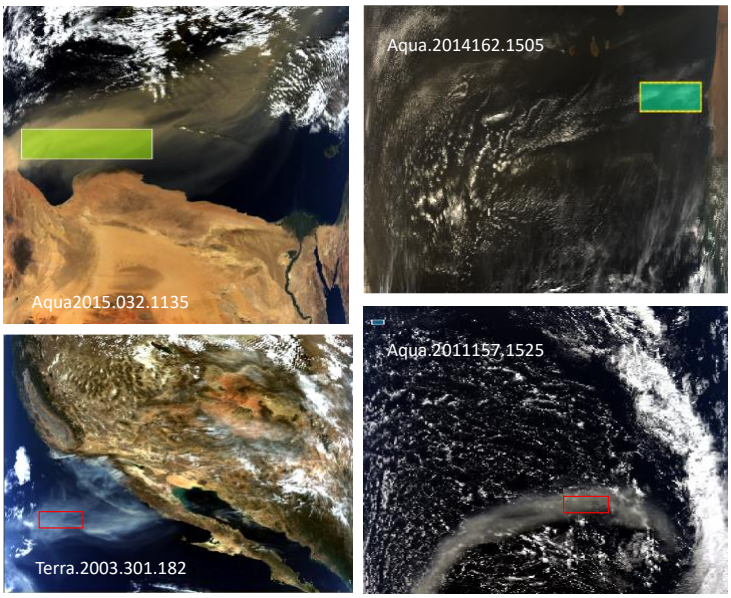

Figure 1. A sample of four out of nineteen granules selected for development of the new dust detection algorithm. Upper left: heavy dust plume. Upper right: diffuse dust mixed with clouds. Lower left: heavy smoke plume. Lower right: smoke plume.

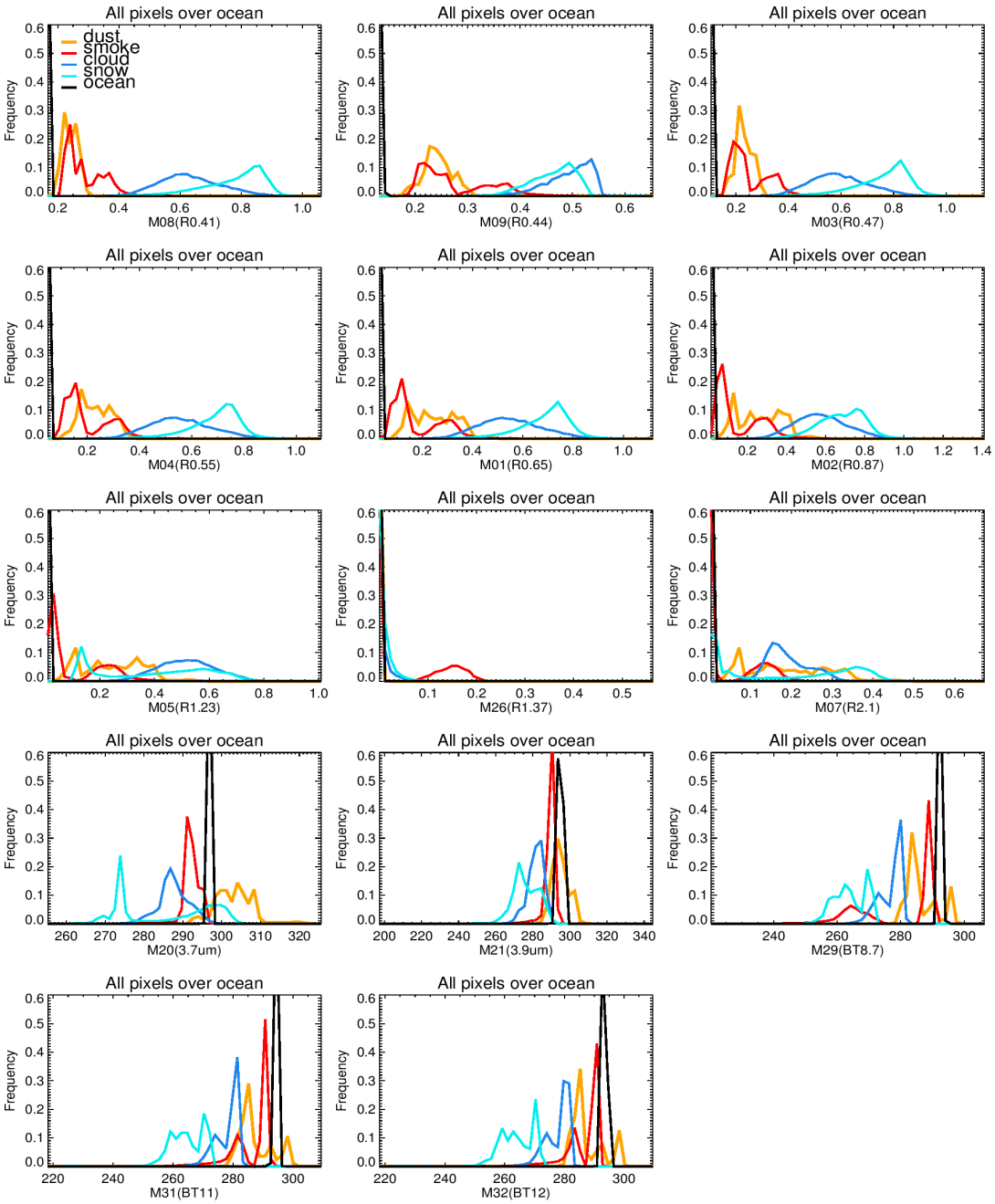

Figure 2. Probability distribution functions of reflectivity for wavelengths 0.41 μm to 2.1 μm and brightness temperature for wavelength greater than 2.1 μm for selected MODIS bands commonly used in single band dust tests. The pixels for difference scenes are manually selected from 19 granules over ocean. The MODIS band number and wavelength in micrometer (starts with R or BT in parenthesis) are shown along the x-axis. The 5% and 95% of PDF values are shown in Table 3. Note that the scales of axes vary.

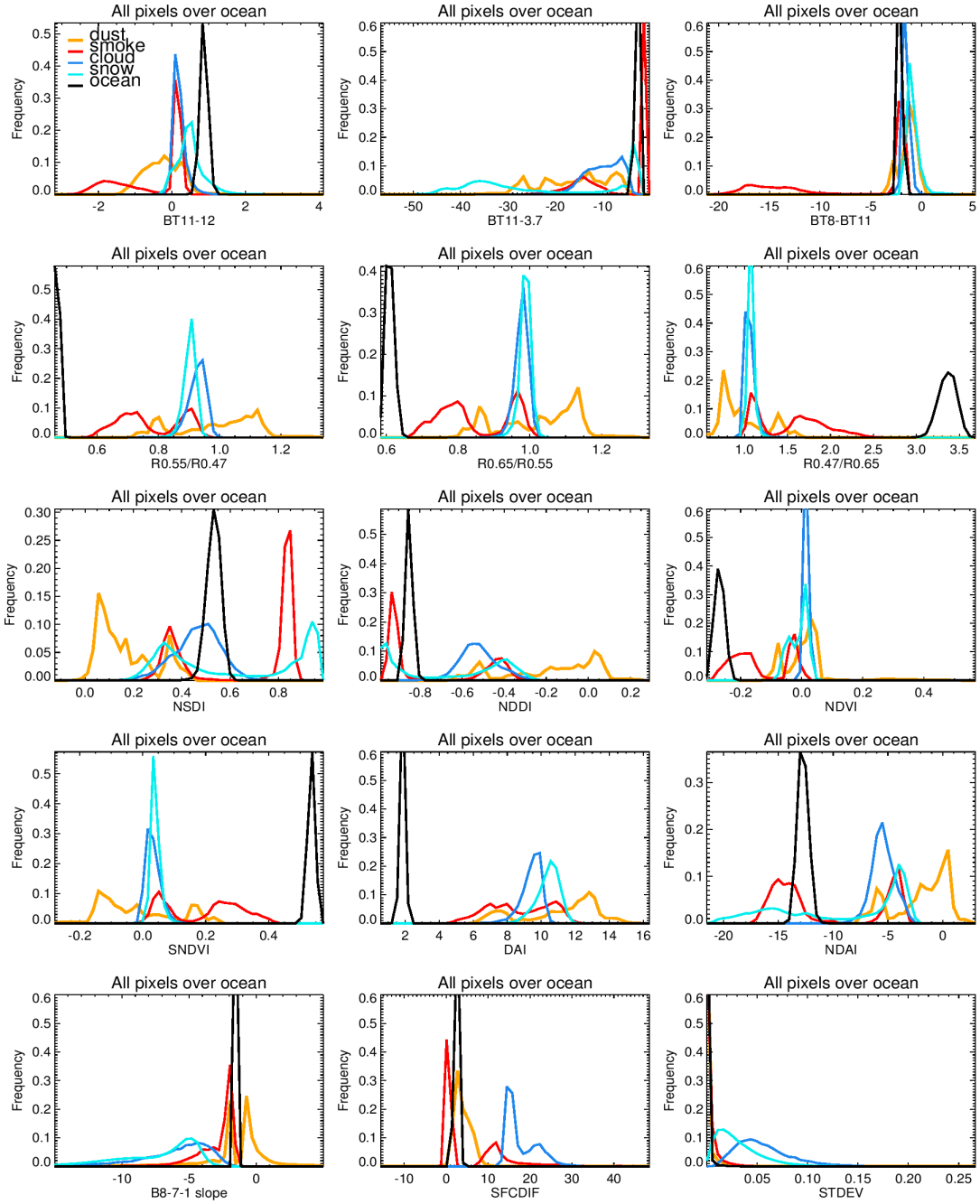

Figure 3. Probability distribution functions of multi-band tests for pixels from different scenes collected from 19 granules over ocean. The definitions of the tests and the 5% and 95% of PDF values are shown in Table 4. The references to the tests can be found in Table 1. Note that the scales of axes vary.

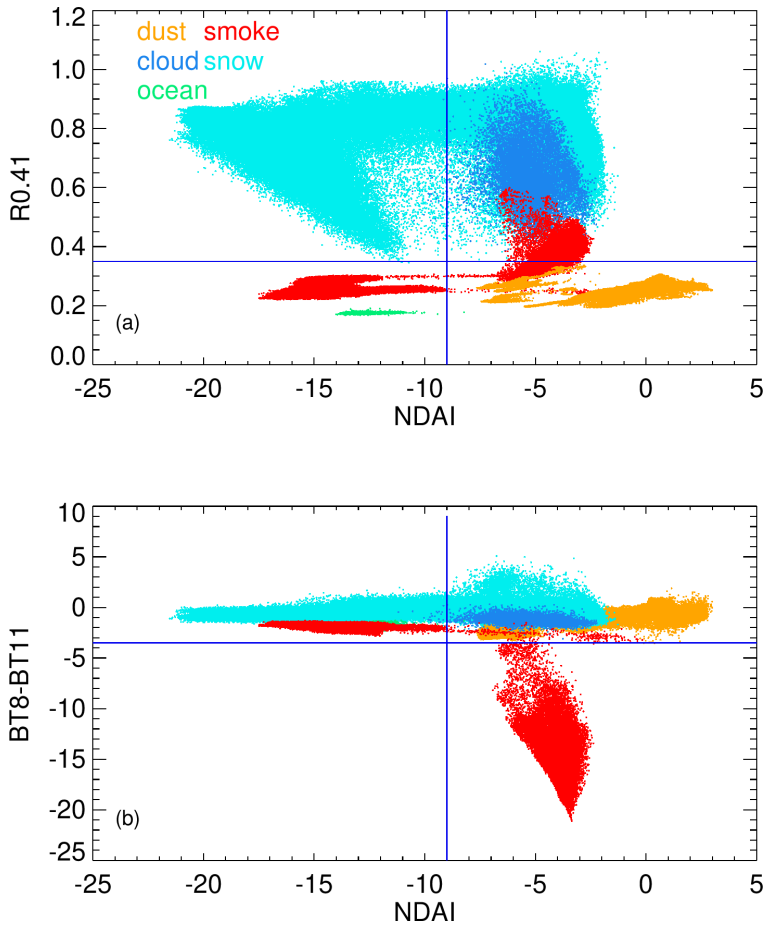

Figure 4. Scatter plots of NDAI with (a) reflectance at 0.41μm, and (b) brightness temperature different at 8.7 μm and 11 μm (BT8-BT11) for pixels collected from 19 images. Pixels from different scenes, i.e., dust, smoke, snow, cloud and clear ocean are indicated with different colors. The blue lines indicate the threshold values for respective tests.

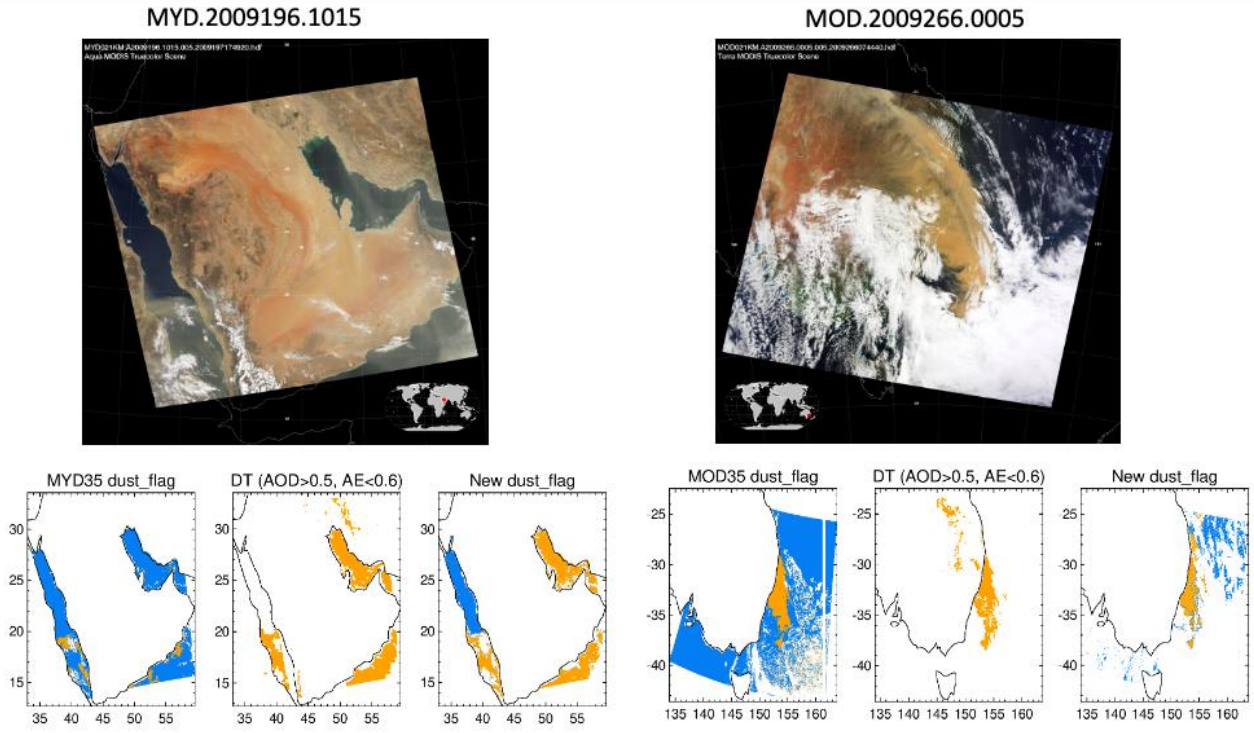

Figure 5. The RGB images of two heavy dusty granules (top) and dust detections from MOD35 dust flag (left), AOD and AE retrievals from DT algorithm (middle), and new dust detection scheme (right) shown below each of the RGB image. The white, blue and yellow colors represent no-test, not-dusty and dusty pixels, respectively.

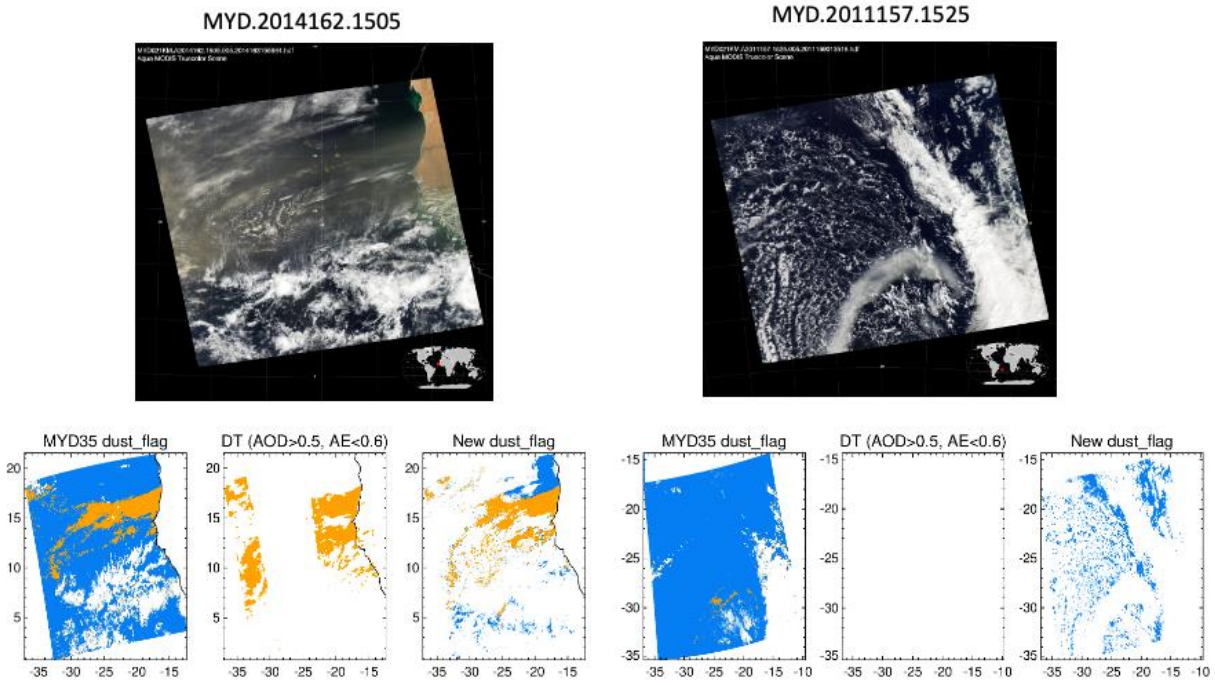

Figure 6. The RGB images of a mixed dusty granules over North Atlantic Ocean (top left) and a smoke granule over South Atlantic Ocean (top right) and corresponding dust detections from MOD35 dust flag (left), AOD and AE retrievals from DT algorithm (middle), and new dust detection scheme (right) shown below each of the RGB image. The white, blue and yellow colors represent no-test, not-dusty and dusty pixels, respectively.

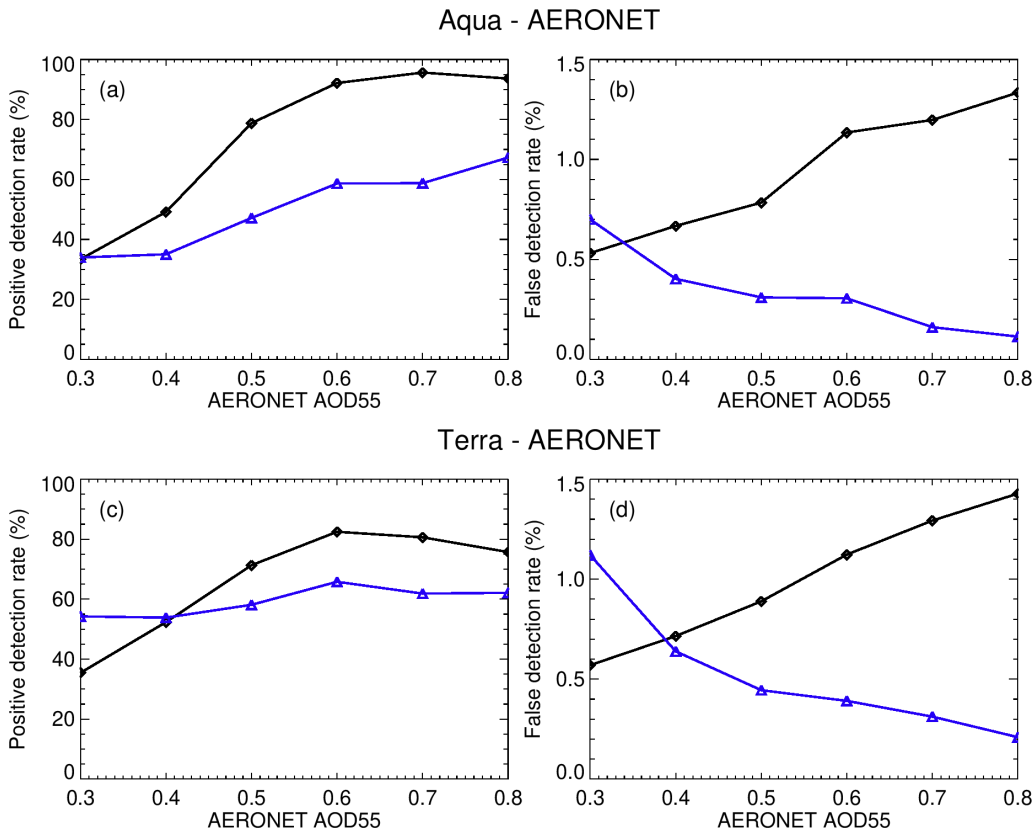

Figure 7. Comparison of new dust detection with dust identified with pairs of AERONET AOD (0.3, 0.4, 0.5, 0.6, 0.7, 0.8) and corresponding AE at (0.8, 0.7, 0.6, 0.5, 0.4, 0.3) thresholds. (a) and (c) are positive detection rates from the new algorithm (black line) for Aqua-AERONET and Terra-AERONET collocated pixels in 2011, respectively, for different pairs of AOD and AE thresholds. (b) and (d) are false detection rates. The blue lines show the positive detection rate in (a) and (c) and false detection rate in (b) and (d) for an after-retrieval dust classification approach using retrieved parameters from the MODIS DT algorithm using AOD and AE thresholds (AOD > 0.5, AE< 0.6, FMF< 0.3) for dust detection.

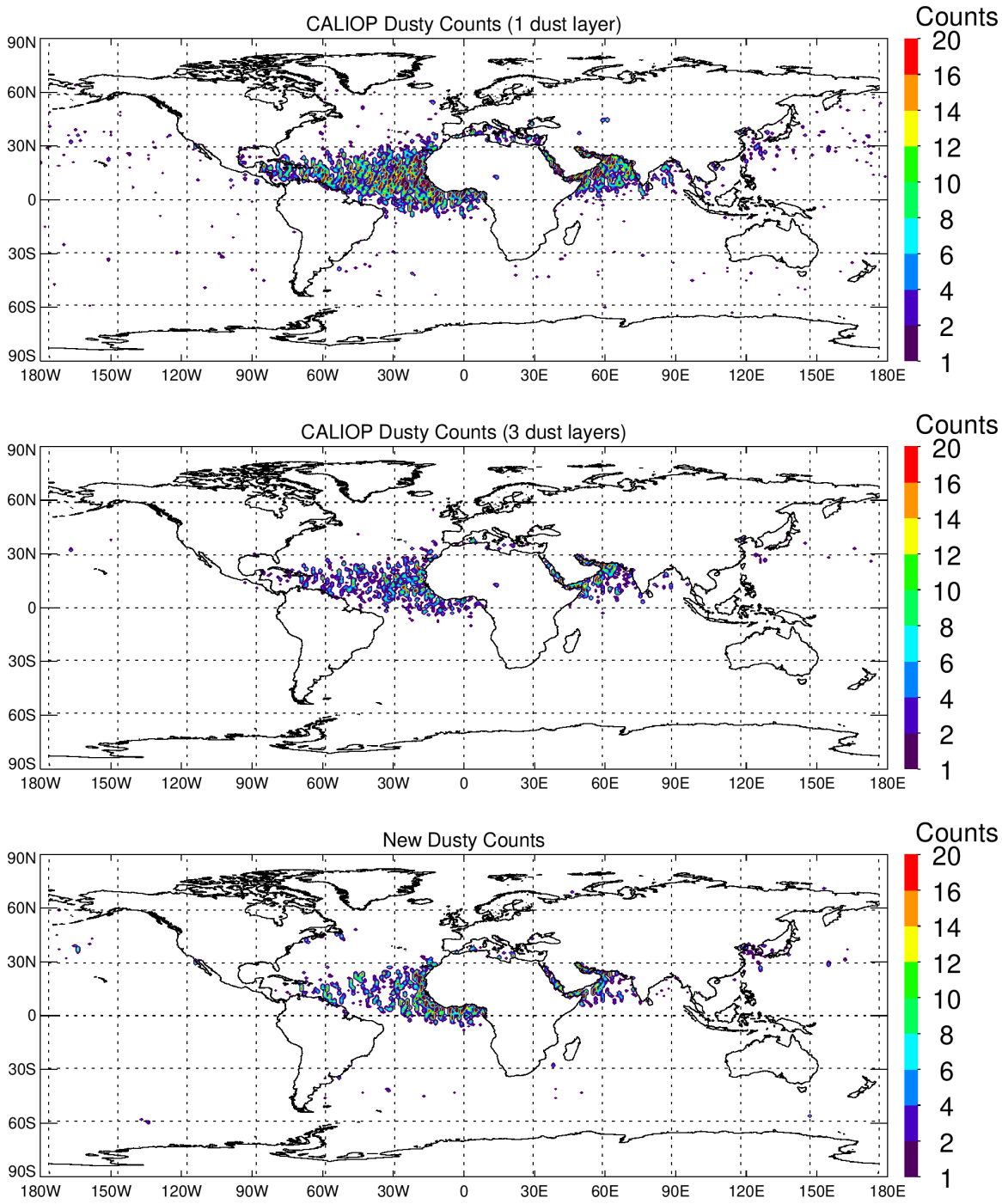

Figure 8. Dust Counts at 1x1° grids based on (a) one CALIOP dust layer, (b) three CALIOP dust layers, and (c) new dust detection algorithm for MODIS AQUA and CALIOP collocated non-cloudy pixels in April and July 2010.

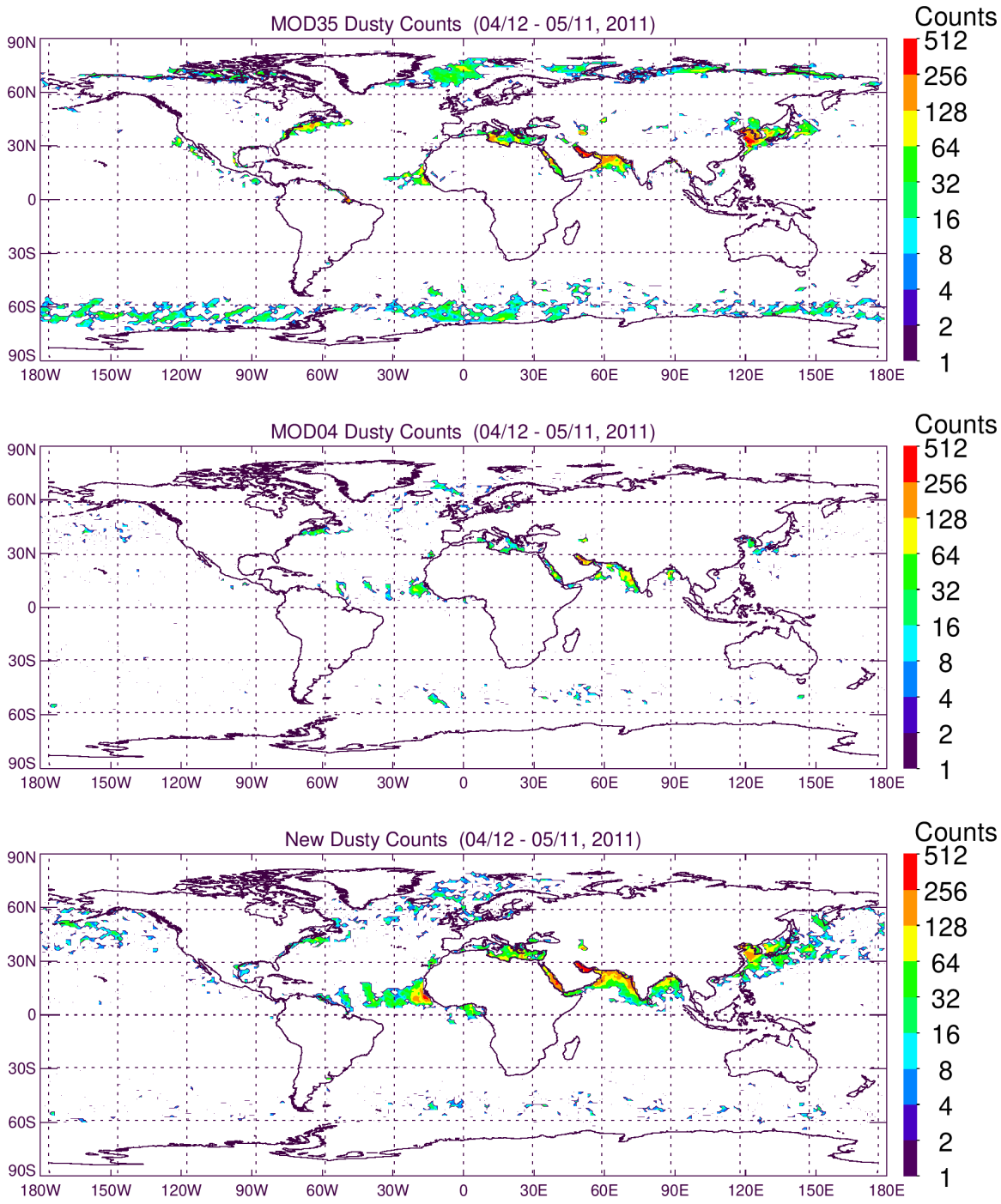

Figure 9: Total number of dusty 10-km pixels in 1x1° grids during April 12-May 11, 2011 based on a) MOD35 dust flag; b) DT retrievals (AOD>=0.5, AE1<0.6, FMF<0.3) and c) new dust detection algorithm.

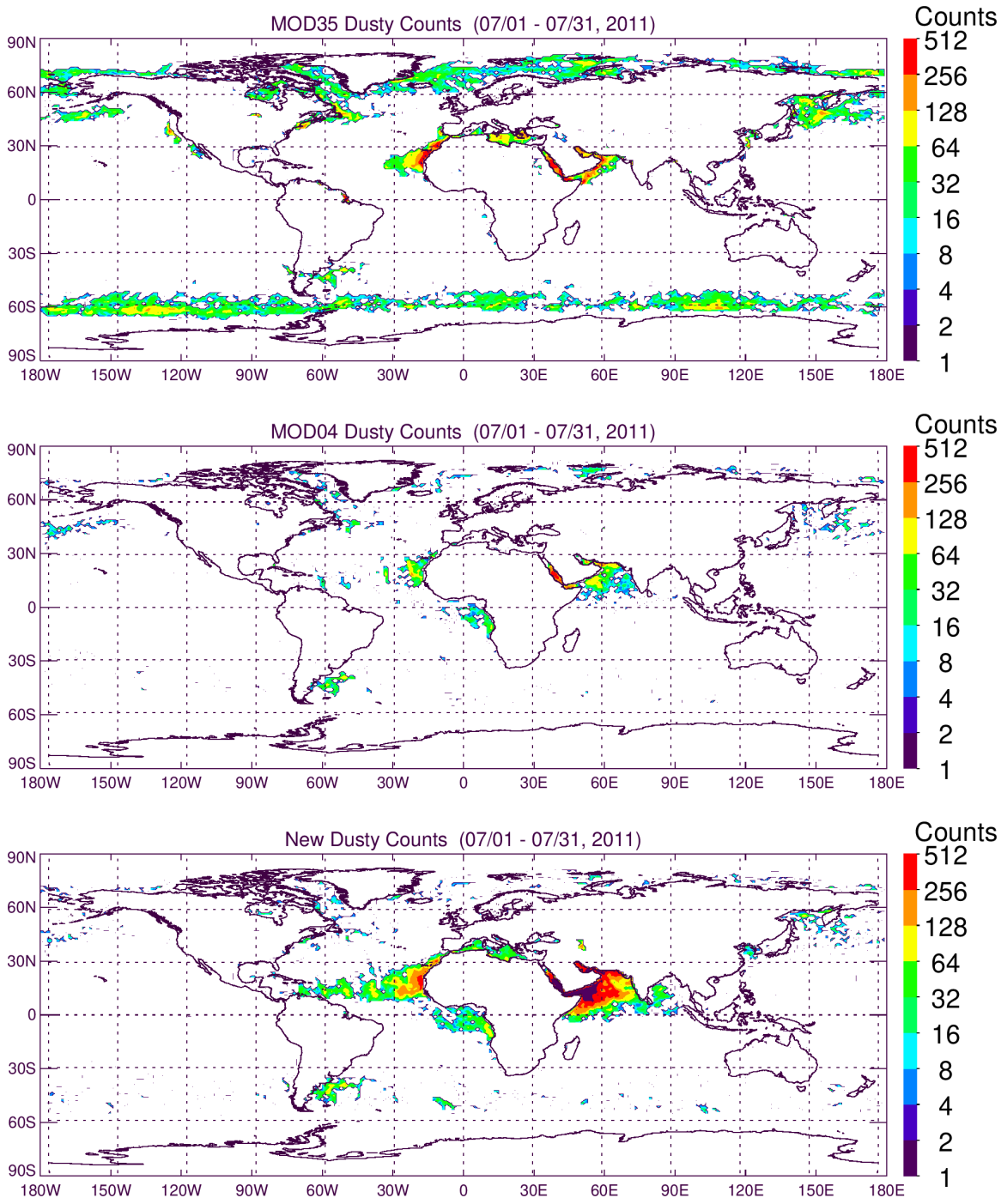

Figure 10: Total number of dusty 10-km pixels in 1x1° grids from July 1-31, 2011 based on a) MOD35 dust flag; b) DT retrievals (AOD>=0.5, AE1<0.6, FMF<0.3) and c) new dust detection algorithm.